

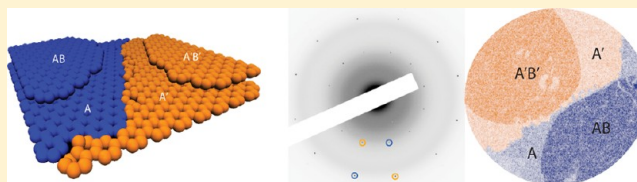
# Layer Number and Stacking Sequence Imaging of Few-Layer Graphene by Transmission Electron Microscopy

Jinglei Ping and Michael S. Fuhrer\*

Center for Nanophysics and Advanced Materials, University of Maryland, College Park, Maryland 20742-4111, United States

**ABSTRACT:** A method based on dark field transmission electron microscopy is developed to quantitatively investigate the layer number and stacking order of multilayer graphene, demonstrated here on multilayer crystalline graphene synthesized by chemical vapor deposition. Our results show that the relative intensities of first- and second-order diffraction spots and contrast in corresponding dark field images are sufficient to identify the layer number and stacking order of graphene with layer number up to seven (7) or more with few-nanometer spatial resolution.

**KEYWORDS:** Graphene, layer number, stacking order, TEM



Graphene, a one-atom-thick layer of graphitic carbon with unique optical, electronic, and mechanical properties,<sup>1–5</sup> is being investigated widely as a promising post-silicon electronic material. The properties of multilayer graphene depend greatly on (i) the number of layers<sup>6</sup> and (ii) the stacking order,<sup>7,8</sup> though facile identification of these characteristics remains a challenge. Optical microscopy is used to measure the layer number of thin graphene samples<sup>9,10</sup> but can be confounded by the presence of other materials on or under graphene. The widely used Raman spectroscopy is an effective method to characterize the layer number and stacking order of exfoliated few-layer graphene.<sup>7,9</sup> However, for graphene samples synthesized by chemical vapor deposition or epitaxial growth on SiC, Raman spectra often do not show clear signatures of Bernal stacked multilayer graphene.<sup>4,11</sup> The above two techniques are also limited in spatial resolution by the wavelength of light. Atomic force microscopy (AFM) may reach quasi-atomic resolution, but absolute measurement of layer number is difficult on continuous graphene samples.

Electron microscopy appears promising for imaging graphene structure on the nanometer scale. Indeed, high angle annular dark field scanning transmission electron microscopy coupled with electron energy loss spectroscopy has been shown to distinguish graphene layer number,<sup>12</sup> and real-space high-resolution TEM images have also been analyzed to distinguish between monolayer and multilayer graphene.<sup>13</sup> Electron diffraction can also give information on graphene layer number and stacking order. Dark-field transmission electron microscopy (DF-TEM) has been used to characterize the polycrystalline structure of graphite or single-layer graphene.<sup>14–16</sup> TEM selected area electron diffraction (SAED) convincingly distinguished monolayer from multilayer graphene<sup>17,18</sup> by the intensity ratio of first-order to second-order diffraction spots being larger or smaller than 1, respectively, and this identification was confirmed by the intensity variation with respect to the tilt angle of the sample holder. A recent work concurrent to this one used dark-field TEM to distinguish layer

number, stacking order, and rotational faults in 1–3 layer graphene.<sup>19</sup>

Here we expand upon the use of SAED patterns and DF images to identify graphene layers and stacking structures. We use a kinematic model to predict the first- and second-order diffraction intensities of multilayer graphene of arbitrary stacking (arbitrary number of layers on A, B, or C sites of the hexagonal lattice). For simple samples (layer number  $n \leq 3$ ), the intensity ratios of first- and second-order SAED spots measured match with theory and real-space DF images are also used to produce maps of layer number contrast with few-nanometer spatial resolution. For complex heterogeneous multilayer graphene samples with layer number  $n \leq 7$ , our method using contrast in DF images unambiguously distinguishes layer-number and stacking-order differences, and the contrast agrees quantitatively with theory. We find that multilayer graphene exhibits Bernal (ABAB...) or rhombohedral (ABCABC...) stacking correlations across multiple layers.

We studied two types of graphene samples prepared by chemical vapor deposition (CVD). Sample type I is grown on 25  $\mu\text{m}$  thick high purity copper foil (99.999%) at 1040  $^{\circ}\text{C}$  in an ambient-pressure furnace.<sup>20,21</sup> The sample is annealed for 30 min under flowing argon (430 sccm) and hydrogen (170 sccm) to remove oxide impurities and increase copper grain size. Then, 10 sccm methane gas is added for 8 min and many-layer graphene is deposited. Then, the sample is annealed in argon/hydrogen with the same temperature and gas flow rates for 30 min and then cooled down. The average number of layers can be controlled by the hydrogen etching duration. From SAED studies, we determine that the multilayer graphene crystallites grown by this method in most cases ( $\sim 95\%$ ) show crystallographic alignment among all the layers. Rare overlap of

**Received:** May 22, 2012

**Revised:** July 18, 2012

**Published:** August 8, 2012

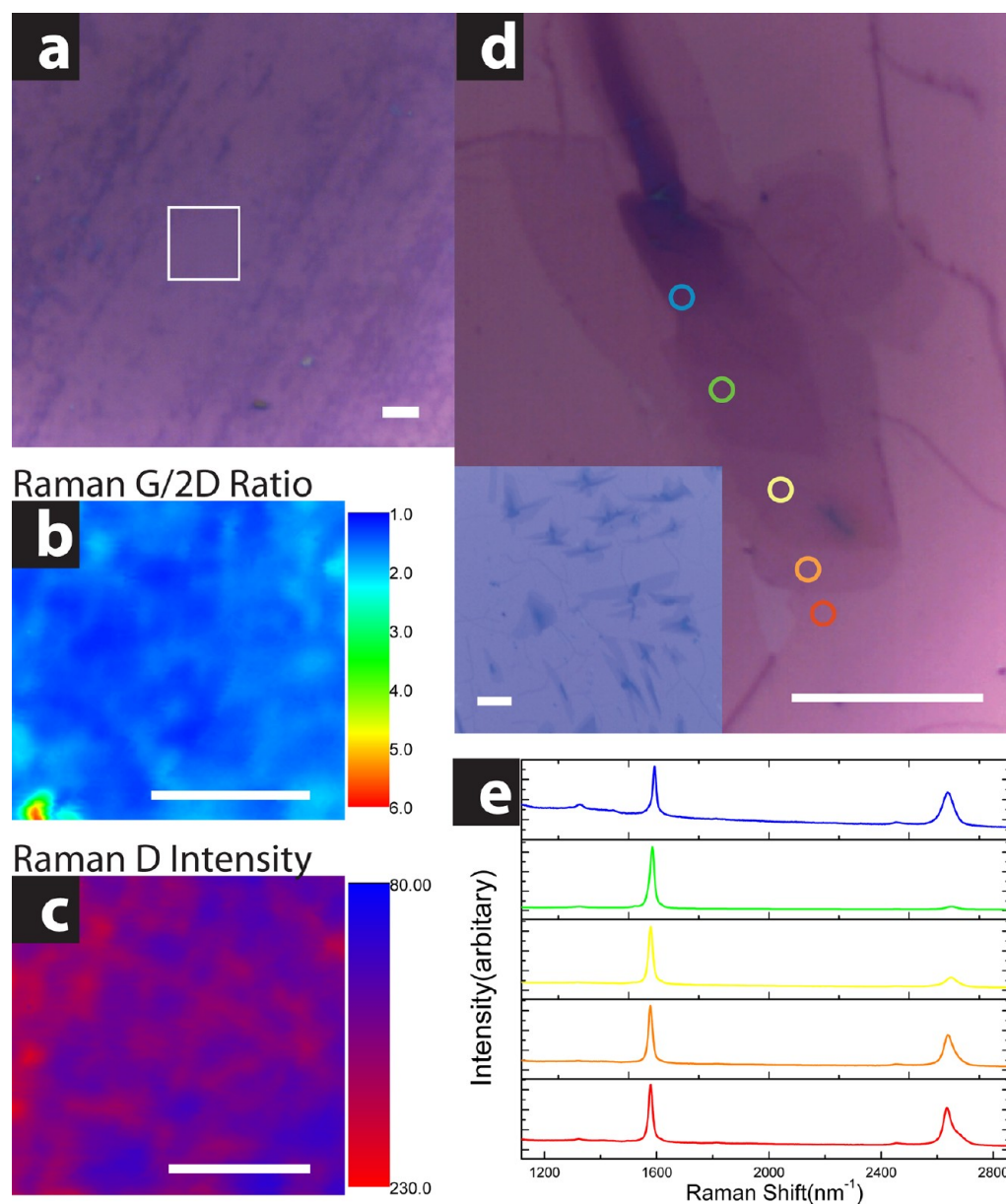


**Figure 1.** Optical micrographs (a) of etched graphene sample type I on 300 nm SiO<sub>2</sub>/Si substrates. Raman mappings (b, c) of the G/2D peak height intensity ratio (b) and D peak intensity (c) of graphene in the areas enclosed by the white square in part a. The white scale bars in parts a, b, and c indicate 5  $\mu$ m. Two examples of the multilayer structure of sample type II are shown in part d and the inset. The scale bars are 10  $\mu$ m. Raman spectra (e) taken in positions indicated by colored circles in part d whose size reflects the size of the laser spot.

graphene layers with different orientations is identified by Moiré patterns in DF images.

We use a four-step method to transfer synthesized graphene on copper (sample type I) to substrates: (1) two layers of poly(methyl methacrylate) (PMMA, MicroChemCorp PMMA 950 A4) are spin coated onto graphene with a speed of 6000 rpm for 45 s; (2) the coated sample is immersed in CE-100 (Transene) copper etchant for 5 min and rinsed in deionized water so that graphene on the uncovered side of the copper foil is removed; (3) the sample is immersed in CE-100 at room temperature for sufficient time so that only PMMA and attached graphene is left; (4) the PMMA with attached graphene is rinsed in deionized water and then transferred to a silicon dioxide wafer or silicon TEM sample holders with a 1.0 mm  $\times$  1.0 mm window covered by 50 nm thick silicon nitride membrane. To remove PMMA, samples are annealed for 4 h at

400  $^{\circ}$ C under flowing argon (300 sccm) and hydrogen (700 sccm). No noticeable changes are observed by scanning electron microscopy for graphene single-crystal flakes annealed under the same conditions, indicating that no additional etching takes place during the 400  $^{\circ}$ C anneal.

Sample type II consists of graphene synthesized on platinum foil in an ambient-pressure CVD furnace.<sup>22</sup> The growth conditions are modified from the sample type I recipe as follows: during growth, the gas mixture is hydrogen (700 sccm), argon (0), and methane (5 sccm). Transfer of graphene from platinum follows the method of ref 22: electrolysis in 1 M NaOH solution is used to “peel” the graphene with PMMA off the platinum. This method makes the reuse of platinum substrate possible and diminishes the metal residues on graphene samples greatly.<sup>22</sup> The grain size of the graphene obtained by this method exceeds 100  $\mu$ m. The graphene is

largely single layer, but small multilayer regions are found, which we study below.

Figure 1 shows optical micrographs (a) and Raman maps using 633 nm incident laser light (b, c) of etched graphene sample type I on 300 nm SiO<sub>2</sub>/Si substrates. The Raman G/2D peak height intensity ratio (b) corresponds qualitatively to layer number, while the Raman D peak height intensity map (c) reflects the presence of graphene edges.<sup>23</sup> Here, large D peak intensity roughly correlates with changes in the G/2D ratio and the D peak mapping is also consistent with the grain size observed in DF-TEM of  $\sim\mu\text{m}$ . Figure 1d,e shows multilayer regions and Raman spectra of sample type II. Both sample types in Figure 1 clearly show that Raman spectroscopy is inadequate to resolve the detailed structure of these graphene samples and may even give misleading layer-number information; for example, the G/2D ratio varies nonmonotonically with thickness in Figure 1e.

We now discuss the expected variations in SAED patterns and DF images for graphene of different layer number and stacking sequence, using kinematic theory and assuming all carbon atoms lie in a 2d plane, expected to be an excellent approximation for up to tens of layers of graphene.<sup>14</sup> Electron diffraction intensity is a product of two factors:  $I = I_0 \times \xi$ . The atomic scattering intensity  $I_0$  arises from the electronic structure of the carbon atom. The modulation term  $\xi$  contains crystallographic information about the graphene lattice. For 100 keV accelerating voltage, which is used in our experiment to minimize irradiation damage and give enough contrast, we use 4.49 for  $I_{01}/I_{02}$ , the intensity ratio of atomic scattering by electrons with transverse wave numbers corresponding to the first two orders of the diffraction pattern.<sup>24</sup> This value agrees with previous experimental results<sup>17</sup> and that obtained from our monolayer graphene sample.

Table 1 shows some values of  $\xi_1$  and  $\xi_2$  for different layer numbers and structure models (stacking sequences). The intensities of the first- and second-order diffraction spots are proportional to  $\xi_1$  and  $\xi_2$ . We assume that there are three possibilities for stacking one graphene layer: if the two atoms in the graphene unit cell are labeled A and B, the next layer may have its atom A stacked over A in the first layer, over atom B in the first layer, or over the hexagon center in the first layer. These three positions are conventionally called A, B, and C, respectively, and the most favorable arrangement in graphene is "ABAB..." stacking, or Bernal stacking, though local regions of rhombohedral "ABCABC..." stacking may be found in graphite.<sup>7</sup> Since in our model the diffraction intensities are only sensitive to the total number of A, B, and C atoms, we denote the structure model with three numbers indicating the number of graphene layers in each of the three possible positions.

As seen in Table 1,  $\xi_2$  varies quadratically with layer number. Thus, the intensity of the second-order diffraction spots alone is sufficient to identify layer number. We will exploit this below to produce a qualitative mapping of layer number in graphene by DF imaging using the second-order diffraction spot. In the case of  $\xi_1$ , and hence first-order diffraction spot intensity, the magnitude depends on layer number and structure. However, there are degeneracies, such as for the monolayer and bilayer. Thus, the ratio of first- to second-order intensities  $I_1/I_2$  is used as an indicator of stacking order;  $I_1/I_2$  is evaluated for 100 keV incident electrons and listed in Table 1.

Figure 2 plots  $\xi_1$ ,  $\xi_2$ , and  $I_1/I_2$  as a function of layer number with different structure models indicated. Single layer graphene (and all "AA" stacked graphene) has the highest  $I_1/I_2$  ratio of

**Table 1. Diffraction Pattern Parameters for Various Structure Models<sup>a</sup>**

layer number	structure model	$\xi_1$	$\xi_2$	$I_1/I_2$
1	1	2	8	1.12
2	1,1	2	32	0.28
3	1,2	6	72	0.37
	1,1,1	0		0
4	1,3	14	128	0.49
	2,2	8		0.28
	1,1,1	2		0.07
5	1,4	26	200	0.58
	2,3	14		0.4
	1,3,1	8		0.31
	2,2,1	2		0.04
6	1,5	42	288	0.65
	2,4	24		0.37
	3,3	18		0.28
	1,1,4	18		0.28
	2,3,1	6		0.09
	2,2,2	0		0.4
7	1,6	62	392	0.71
	2,5	38		0.44
	3,4	26		0.30
	1,5,1	32		0.37
	2,4,1	14		0.16
	3,3,1	8		0.09
	3,2,2	2		0.02

<sup>a</sup>The notation for the structure models is described in the text.  $\xi_1$  and  $\xi_2$  are the first- and second-order diffraction pattern modulation terms. The intensities of the first- and second-order diffraction spots are proportional to  $\xi_1$  and  $\xi_2$ .  $I_1/I_2$  is the expected ratio of the intensity of first- and second-order diffraction spots at 100 keV.

1.12. Bernal stacked graphene tends to converge to a ratio of 0.3, and rhombohedral graphene, to a ratio 0 (i.e., the first-order spot is missing). Thus, for layer number  $n \leq 3$ , the ratio clearly identifies all possible layer numbers and structure models. For large layer number, the ratio gives some contrast between regions of differing layer number (especially differing by one layer) and is particularly sensitive to the presence of stacking faults.

We now give a quantitative example of our imaging technique. Figure 3a shows a typical SAED pattern which indicates that two different crystallographic orientations (two grains) are present. Four raw DF images in Figure 3b correspond to the first- and second-order diffraction spots for the two crystallographic orientations (orange or blue circles in part a). The data of raw DF images are converted to grayscale, and the areas of graphene are isolated by applying a threshold on the grayscale mapping. They are then colored, orange or blue respectively corresponding to the two crystallographic orientations, with intensity corresponding to the grayscale value, and merged and inverted to generate Figure 3c (for DF images corresponding to first-order spots) and Figure 3d (second-order spots). On the basis of the one-to-one correspondence between SAED patterns and DF images, regions with different colors (orange, blue) represent graphene with different orientations. The first-order DF image (Figure 3c) shows no layer number contrast, as expected from  $I_1$  in Table 1, while the second-order DF image shown (Figure 3d) demonstrates clear contrast within each crystallographic region. As Table 1 indicates, the second-order SAED pattern, and thus



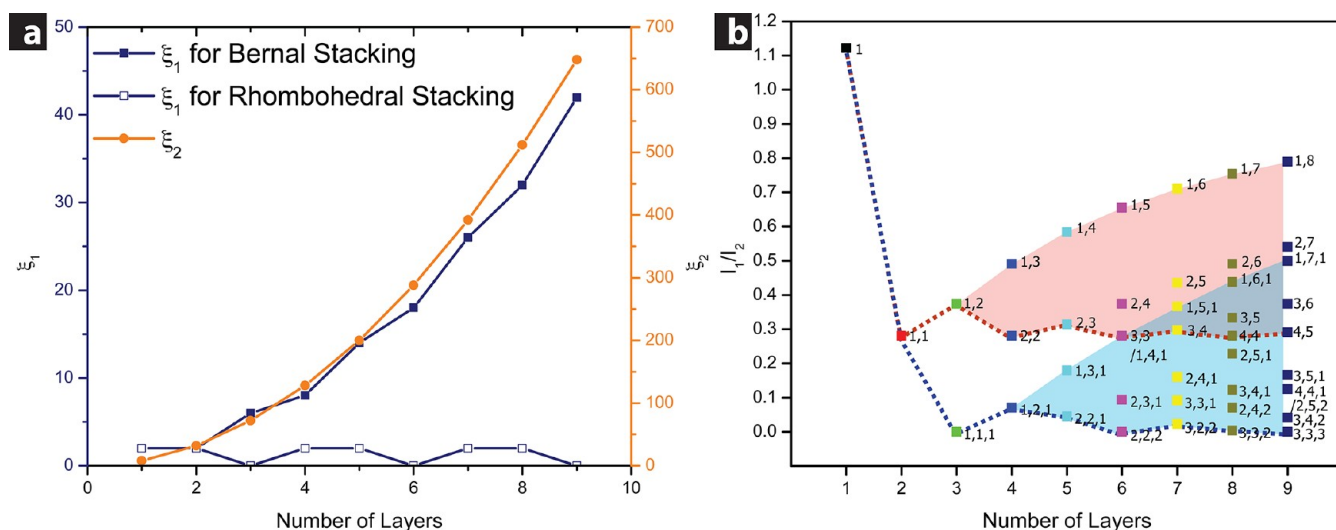


**Figure 2.** The curves in part a show  $\xi_1$  for Bernal and rhombohedral stacking and  $\xi_2$  obtained from Table 1. Note the layer-number-identification ability of  $\xi_2$  despite the stacking order. The squares in part b are electron diffraction intensity ratios for first- and second-order diffraction spots  $I_1/I_2$  as a function of layer number. The structural model is denoted using the notation described in the text. The dashed red line connects structure models representing Bernal stacking, and the dashed blue line connects structure models representing rhombohedral stacking. The shaded pink and blue regions enclose structure models containing two elements (AB) and three elements (ABC), respectively.

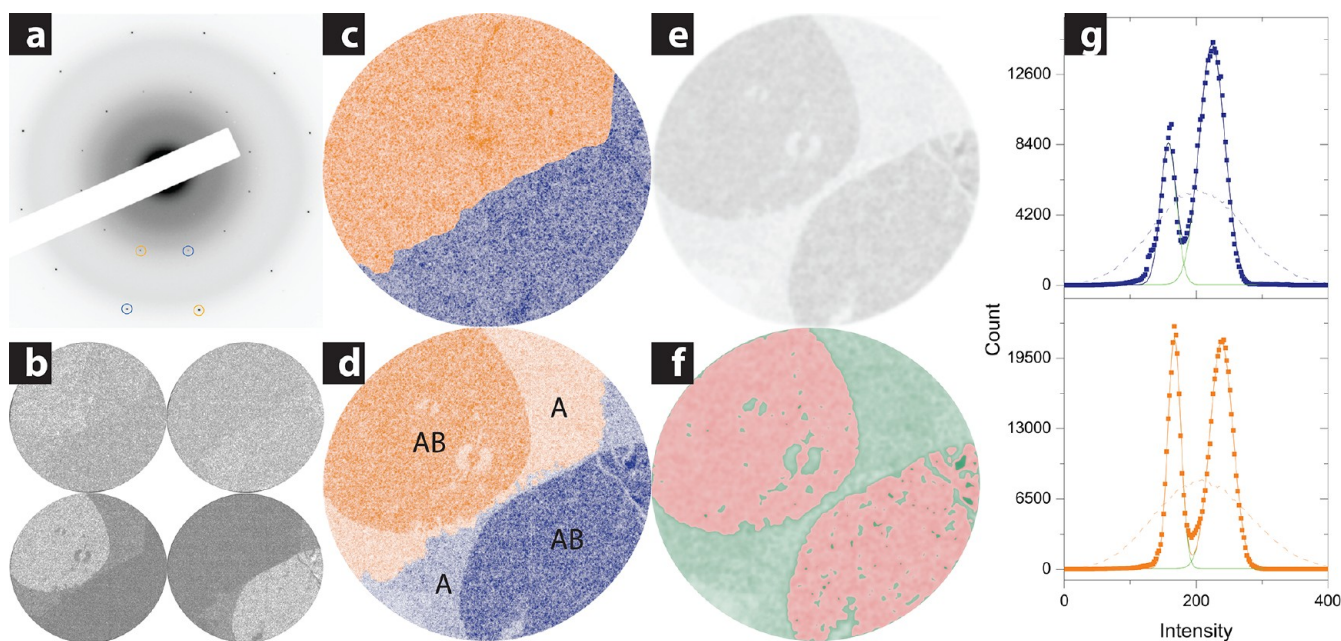


**Figure 3.** SAED pattern (a) and corresponding raw DF images (b) of a sample hydrogen etched for 30 min. Combined dark field images (c, d) for first-order (c) and second-order (d) diffraction spots. Color corresponds to crystallographic orientation, as indicated in part a. The indices in part d are structure models. (e) Grayscale image of the ratio of first-order to second-order diffraction intensity. (f) Same image as part e, colored to indicate areas of single-layer graphene (green) and Bernal stacked bilayer graphene (red). (g) Histograms of the intensities of the DF image (d) for blue (upper panel) and orange (lower panel) crystallographic orientations. The dashed lines indicate histograms of the raw image, and the solid points indicate histograms after Gaussian filtering the images at 4.8 nm. The solid lines are fitted to two Gaussians, with individual Gaussian components indicated by green lines. The diameters of all DF images are 1  $\mu\text{m}$ .

its corresponding DF map, is sufficient to distinguish layer number. Hence, dark and light regions in part d correspond to thicker layer and thinner regions, respectively.

In order to generate a map of layer number contrast alone, the raw second-order DF images in part b are added and then Gaussian filtered with a 6 pixel variance (4.8 nm), resulting in image e. A histogram of the intensities in part e shows two well-resolved peaks, indicating two contrast levels are well-resolved at 4.8 nm resolution. (The histogram of the raw image shows

only one peak.) Setting the threshold between the two peaks allows the image to be colored corresponding to the areas of different layer number (Figure 3f). Moreover, the histogram also measures the areas of graphene with different layer numbers but the same orientation, which are proportional to the areas enclosed by each peak, and the total area of graphene with each orientation, which is proportional to the area enclosed by the whole fitting curve.

We now determine the layer number and structure model for the different regions of the sample in Figure 3. The background of the SAED pattern is eliminated by a rolling-ball algorithm with ball radius 50 pixels, and intensities of SAED spots are obtained by integration over Gaussian peaks and then spots of the same order are averaged and the ratio  $I_1/I_2$  is indicated in Table 2. A parameter  $\beta^{(i)}$  that indicates the area portion of

**Table 2. Determination of the Structure Model of the Graphene Samples Shown in Figure 3<sup>a</sup>**

region	$I_1/I_2$		$I_1^{(o)}/I_1^{(b)}$		$I_2^{(o)}/I_2^{(b)}$		structure model
	exp.	theo.	exp.	theo.	exp.	theo.	
orange	0.39	0.38	1.54	1.51	1.34	1.37	1(36%) &1,1(64%)
blue	0.34	0.35					1(27%) &1,1(73%)

<sup>a</sup>The experimental quantities  $I_1/I_2$  and  $I_k^{(m)}/I_k^{(n)}$  and the theoretical results for the structure model are shown. The sign "&" in the structure model column represents the coexistence of two or more structure models with the same crystal orientation. Percentages in the structure model column represent the fraction of area with that structure determined experimentally from histograms (Figure 3g).

graphene with layer number index  $i$  is evaluated from the area of peaks obtained from histograms (Figure 3g). For orientation-identical graphene with two different layer numbers, we have

$$\frac{I_1}{I_2} = \frac{\beta^{(i)}I_1^{(i)}/I_1^{(j)} + 1 - \beta^{(i)}}{\beta^{(i)}I_2^{(i)}/I_2^{(j)} + 1 - \beta^{(i)}} \times \frac{I_1^{(j)}}{I_2^{(j)}} \quad (1)$$

The theoretical values of  $I_1/I_2$  in Table 2 match the experimental data very well.

The quantity  $I_1/I_2$  may not be accurate enough to identify layer numbers of complicated layer-mixed and/or many-layer graphene because (i) there is always more than one possible combination of structure model having values close to  $I_1/I_2$  and (ii) the distribution of  $I_1/I_2$  becomes denser as the layer number increases, as shown in Figure 2. However, if there are multiple grains of different orientations, additional information is possible by comparing  $I_k^{(m)}/I_k^{(n)}$ , the ratios of intensity from SAED spots of grains  $m$  and  $n$  with the same order  $k$ . The additional ratios are shown in Table 2 for the sample shown in Figure 3; again, the theory matches with the experiment well.

Second-order DF images are also used to investigate our samples on a larger scale, and we find thin graphene layers at the edges of crystallites, implying that etching always takes place at the boundaries between graphene single crystals, similar to the observation in Figure 3. This demonstrates the usefulness of our technique for understanding the growth and etching processes in graphene.

We now analyze a more heterogeneous graphene structure in sample type II. Figure 4a and b shows stepped-pyramid structures of small graphene crystallites observed occasionally on samples of type II. While the bright field images (Figure 4a and b) show vague contrast, the second-order dark field images (Figure 4c and d) clearly distinguish the presence of many discrete layer number regions with sharp boundaries. Interestingly, the first-order dark-field images show regions of different contrast within each terrace of constant second-order contrast, which we interpret as regions of different stacking order as verified below. Note that in one sample (Figure 4a,c,e)

there is an additional single graphene layer covering the upper portion of the image which is slightly rotated with respect to all the other layers, producing a Moiré pattern (this was verified by noticing that the Moiré pattern orientation rotated according to the diffraction spot used to produce the image).

We assign stacking orders to the various regions in Figure 4 as follows. We notice that for a given second-order intensity there are at most two different first-order intensities. Therefore, we assume that there are only two types of stackings: Bernal (AB) and rhombohedral (ABC). We assign the higher-intensity first-order areas as Bernal stacked and lower-intensity areas as rhombohedrally stacked. The stacking assignments are denoted in Figure 4e and f. In Figure 4e, there is a sharp boundary (purple arrow) between rhombohedrally stacked graphene on the lower left and Bernal stacking on the upper right. The first-order intensity grows monotonically with layer number for the Bernal-stacked region but is low and non-monotonic in layer number for rhombohedrally stacked graphene, in qualitative agreement with Figure 2a. Similar but less sharply defined regions of rhombohedral stacking are observed in Figure 4f.

We now analyze the first- and second-order diffraction contrast quantitatively. Figure 5a, b, c, and d shows line profiles along the colored lines in Figure 4c, e, d, and f, respectively. We take averages over the regions denoted by horizontal lines (the vertical position of the line shows the average) which are identifiable on the dark-field images as areas of uniform contrast. Figure 5e–h shows the average contrast values for each region in Figure 5a–d plotted versus the expected contrast (see Figure 2a). There is an offset in the experimental values mainly due to a diffuse background in the dark-field images due to the presence of the silicon nitride membrane. For this reason, we used the diffraction contrast directly instead of the quantity  $I_1/I_2$ . The linear relationship in Figure 5e–h indicates agreement between experiment and theory. The experiment shows the fine details of the theory: The second-order intensity varies quadratically with layer number (Figure 5e,g). For Bernal and rhombohedral stacking within the same layer number (Figure 5h; ABCA vs ABAB), the experiment shows the expected relative intensities. For Bernal stacking, the first-order diffraction intensity (Figure 5f) rises with layer number monotonically but nonuniformly [for example, ABA (6) and ABAB (8) and ABABA (14) and ABABAB (18) are relatively closely spaced in intensity]. We note that, because of the background, absolute layer thickness determinations from measurement of only one or a few structures would be difficult with our technique, but the situation could be significantly improved by suspending the graphene.

We now discuss the observation of different stacking sequences in our graphene samples of type II. The coexistence of rhombohedral and Bernal stacking had been previously observed in Raman microscopy on trilayer graphene. Here we make two new observations: First, we observe that stacking correlations (rhombohedral vs Bernal) persist over several layers (up to seven layers in Figure 4e). This is quite surprising given the weak interlayer interactions in graphene. Second, we observe that most boundaries between rhombohedral and Bernal stacked regions appear to be associated with out-of-plane deformation or wrinkling of graphene (seen as a dark contrast in the second-order dark-field images, Figure 4c and d). This suggests mechanical stress as either a cause or a result of the stacking fault boundary. The very straight boundary between rhombohedral and Bernal stacking seen in Figure 4e appears somewhat unusual compared to the meandering lines



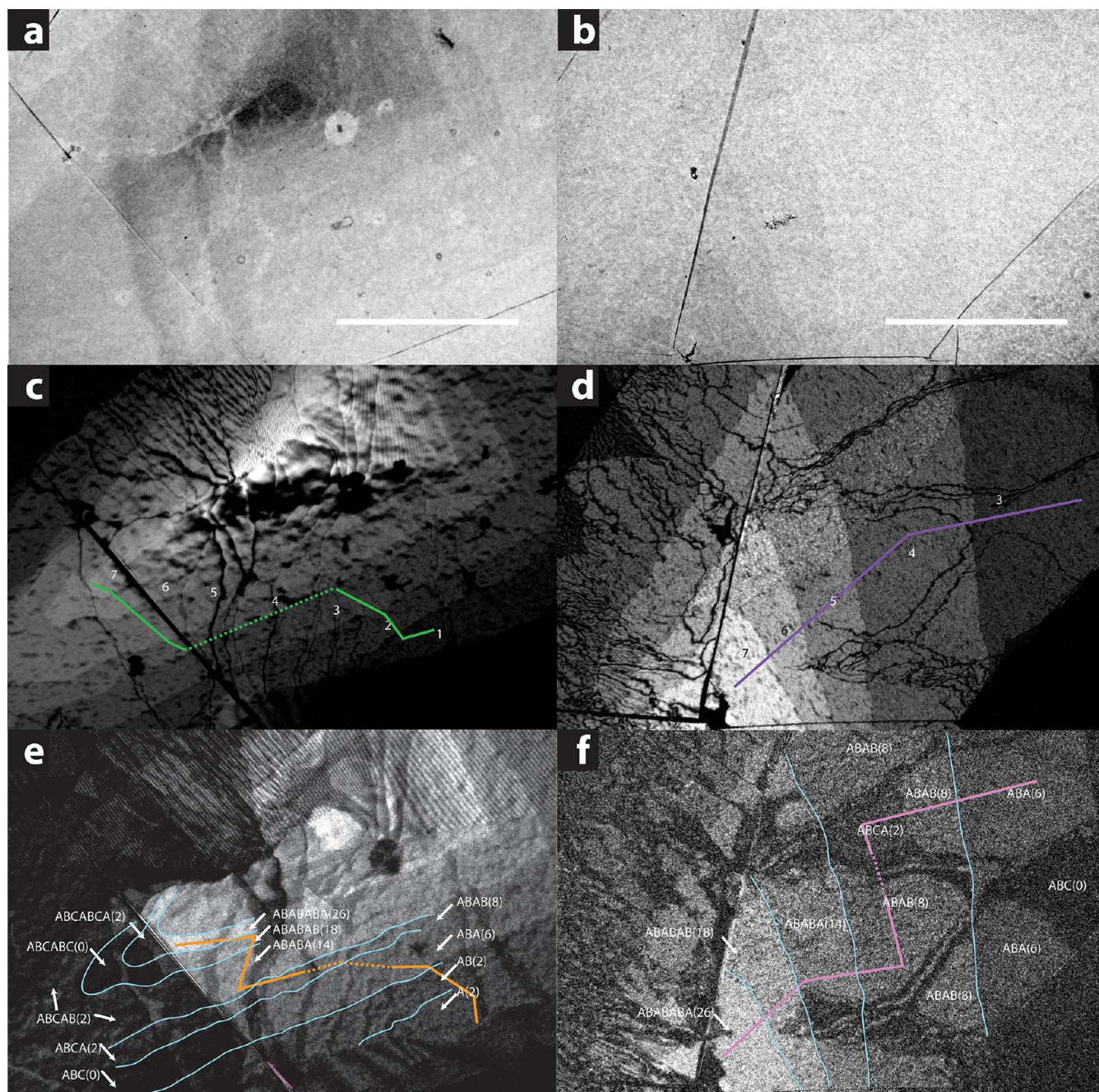


**Figure 4.** Bright-field images (a and b) of two samples of type II that are also investigated with SAED patterns and DF images; the scale bars are 500 nm. The layers are barely distinguished. Second-order DF images (c and d) and first-order DF images (e and f) correspond to parts a and b in the same column with the same scale. The cyan contours in parts e and f are obtained from parts c and d, which are sufficient to give layer number, as labeled. The stacking orders are labeled in parts e and f with values of  $\xi_1$  in parentheses. The boundary of Bernal and rhombohedral stacking in part e is indicated by the purple arrow. The segmented lines in parts c–f correspond to intensity profiles shown in Figure 5.

that we presume are wrinkles; we are unsure of the origin of this feature.

Finally, we address the robustness of our technique to disorder or thermal fluctuations. The high Debye temperature of graphene indicates that corrections to  $I_1/I_2$  due to the thermal Debye–Waller factor are on the order of 1% at room temperature.<sup>25</sup> Static disorder due to, e.g., vacancies or adatoms<sup>26</sup> which shift the atomic positions can lead to a static Debye–Waller factor.<sup>27</sup> However, point defects are easily detectable through the presence of a Raman D band. The Raman D to G intensity ratio is at most 0.3 in our samples (and

often much lower), indicating a point defect concentration of at most 100 ppm,<sup>28</sup> which would lead to corrections to  $I_1/I_2$  on the order of 100 ppm or less. Static disorder is therefore unlikely to significantly modify the analysis of our samples, or any technologically relevant graphene samples with modest disorder.

In conclusion, we have demonstrated a technique using transmission electron microscopy small area electron diffraction and dark-field imaging of first- and second-order diffraction spots to produce real-space images with contrast in graphene layer number and stacking order with few-nanometer



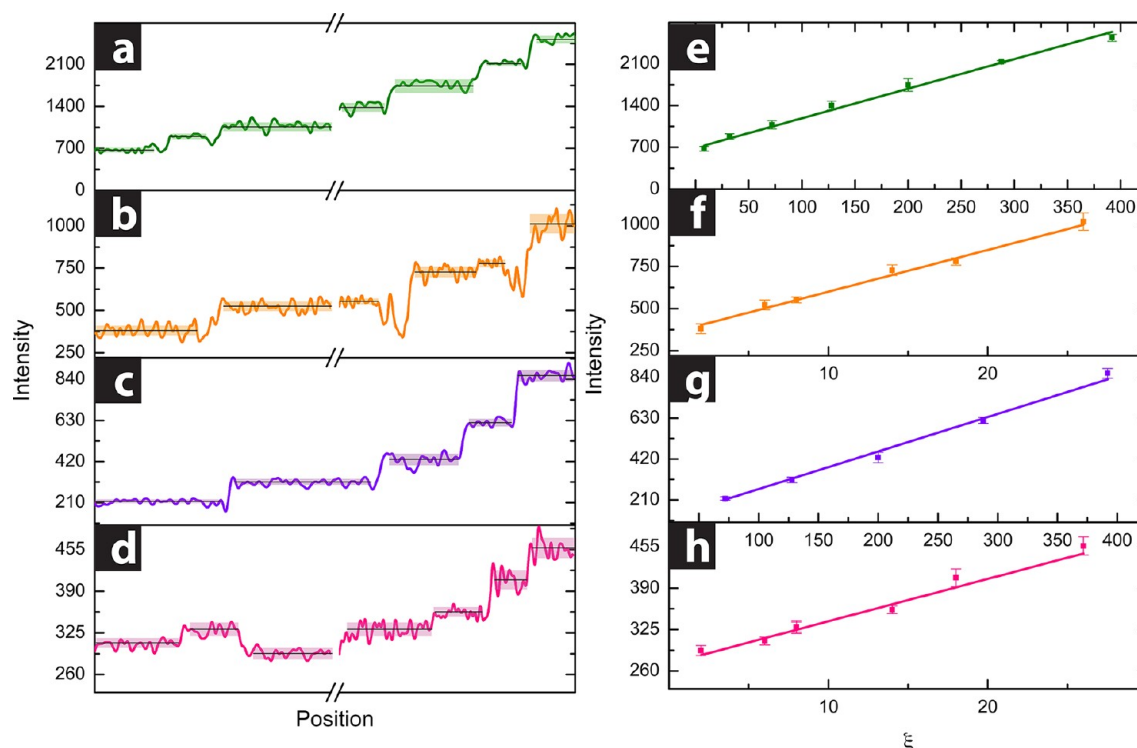


**Figure 5.** Intensity profiles (a–d) correspond to the same-color segmented lines in Figure 4c–f. The break points correspond to the dashed line segments. Horizontal lines and shaded regions denote the mean value and standard deviation of the intensity averaged over each segment. Experimentally determined mean intensities (e–h) as a function of the theoretically calculated  $\xi$  values from Table 1 for the structure assignments indicated in Figure 4c–f. A linear relationship indicates agreement between experiment and theory.

resolution. The heterogeneous multilayer graphene samples are prepared by ambient-pressure chemical vapor deposition on copper or platinum. This extension of the transmission electron microscopy technique fills a needed gap in characterization of multilayer graphene, since probes of layer structure at the nanoscale were not previously available.

## AUTHOR INFORMATION

### Corresponding Author

\*E-mail: mfuhrer@umd.edu.

### Notes

The authors declare no competing financial interest.

## ACKNOWLEDGMENTS

This work was partially supported by the Laboratory for Physical Sciences; the Science of Precision Multifunctional Nanostructures for Electrical Energy Storage, an Energy Frontier Research Center funded by the U.S. DOE, Office of Science, Office of Basic Energy Sciences under Award Number DESC0001160; and the ONR-MURI program. The Shared Experimental Facilities of the University of Maryland MRSEC (NSF grant DMR 05-20741) were used in this research. We acknowledge the support of the 373 Maryland NanoCenter and its NispLab.

## REFERENCES

- (1) Novoselov, K. S.; et al. *Science* **2004**, *306*, 666.
- (2) Lee, C.; Wei, X.; Kysar, J. W.; Hone, J. *Science* **2004**, *321*, 385.
- (3) Kuzmenko, A. B.; van Heumen, E.; Carbone, F.; van der Marel, D. *Phys. Rev. Lett.* **2008**, *100*, 117401.
- (4) Lenski, D.; Fuhrer, M. S. *J. Appl. Phys.* **2011**, *110*, 013720.
- (5) Morozov, S. V.; et al. *Phys. Rev. Lett.* **2008**, *100*, 016602.

- (6) Novoselov, K. S.; et al. *Nat. Phys.* **2006**, *2*, 177–180.
- (7) Lui, C. H.; et al. *Nano Lett.* **2011**, *11*, 164.
- (8) Avetisyan, A. A.; Partoens, B.; Peeters, F. M. *Phys. Rev. B* **2010**, *81*, 115432.
- (9) Ferrari, A. C.; et al. *Phys. Rev. Lett.* **2006**, *97*, 187401.
- (10) Kuzmenko, A. B.; et al. *Phys. Rev. Lett.* **2008**, *100*, 117401.
- (11) Lee, S.; Lee, K.; Zhong, Z. *Nano Lett.* **2011**, *10*, 4702.
- (12) Eberlein, T.; et al. *Phys. Rev. B* **2008**, *77*, 233406.
- (13) Plachinda, P.; Rouvimov, S.; Solanki, R. *Phys. Status Solidi A* **2011**, *208*, 2681.
- (14) Horiuchi, S.; et al. *Jpn. J. Appl. Phys.* **2003**, *42*, L1073.
- (15) Huang, P. Y.; et al. *Nature* **2011**, *469*, 389.
- (16) Kim, K.; et al. *ACS Nano* **2011**, *5*, 2142.
- (17) Meyer, J. C.; et al. *Solid State Commun.* **2007**, *143*, 101.
- (18) Meyer, J. C.; et al. *Nature* **2007**, *446*, 60.
- (19) Brown, L.; et al. *Nano Lett.* **2012**, *12*, 1609.
- (20) Bae, S.; et al. *Nat. Nanotechnol.* **2010**, *5*, 574.
- (21) Li, X.; et al. *Science* **2009**, *324*, 1312.
- (22) Gao, L.; et al. *Nat. Commun.* **2012**, *3*, 699.
- (23) Yu, Q.; et al. *Nat. Mater.* **2011**, *10*, 443.
- (24) Treacy, M. M. *Microsc. Microanal.* **2011**, *17*, 847.
- (25) Chen, R.; Trucano, P. *Acta Crystallogr., Sect. A* **1978**, *34*, 979.
- (26) Banhart, F.; Kotakoski, J.; Krashenninnikov, A. V. *ACS Nano* **2011**, *5*, 26.
- (27) Huang, K. *Proc. R. Soc. London, Ser. A* **1947**, *190*, 102.
- (28) Lucchese, M. M.; et al. *Carbon* **2010**, *48*, 1592.